

# The Streaming Current Detector: A Quantitative Model

CHRISTOPHER A. WALKER, JAMES T. KIRBY, AND STEVEN K. DENTEL<sup>1</sup>

*Department of Civil and Environmental Engineering, University of Delaware, Newark, Delaware 19716*

Received August 22, 1995; accepted March 13, 1996

**The streaming current detector (SCD) is an instrument used for continuous characterization of colloidal surface charge. It measures the alternating current generated by mobile counterions when charged material momentarily adheres to cylinder and piston walls while the piston reciprocates. The utility of the SCD for coagulant control is generally accepted, as evidenced by the estimated one thousand units in service in North America. However, one drawback to this device has been the lack of an exact quantitative model explaining its functioning. This paper provides such a description, relating the generated current to the zeta potential of the characterized material as a function of instrument parameters and solution chemistry. The model, programmed in *Mathematica*, agrees closely with an earlier analytical solution under many conditions. Its inclusion of an inertial term, however, allows behavior of the SCD to be simulated under a more general range of conditions.**

© 1996 Academic Press, Inc.

**Key Words:** streaming current; streaming current detector; zeta potential; annular flow.

## BACKGROUND

The streaming current detector (SCD) was first introduced as a new technology in 1966 (10). In more recent years the device has become widely used in the water treatment industry as a method of continuous, on-line monitoring and of controlling of coagulant dosage (3). It is also used in a number of other applications where colloidal charge is to be altered by a controlled chemical dosage. The device's sensor comprises a piston that reciprocates vertically within a cylindrical housing that is closed at the bottom (Fig. 1). Either the piston or the cylinder is fitted with a pair of electrodes located at axially opposite ends of the annular space between the piston and the cylinder.

Above the narrow annular zone is a reservoir of water containing the charged colloidal material to be characterized. The water may be provided by immersion of the sensor in a batch sample or by provision of a flow-through line for continuous sampling from an ongoing process (4, 5). Fluid carrying charged colloidal material (and associated counterions) is drawn into and out of the annular space as the piston

moves up and down. These charged particles are momentarily immobilized on the surfaces of the piston and the cylinder. As the fluid motion forces mobile counterions in the double layer past these immobile particles, half-reactions at the electrodes generate the streaming current as an alternating current which is directly related to the charge on the particles (3, 10). Electrical circuitry capable of phase-sensitive amplification and rectification of the current can then provide a continuous reading that characterizes the polarity and magnitude of colloidal charge in the sample.

The device differs from the classical means of measuring streaming potential or current in that the dead-ended chamber provides electrical isolation of the cell while still allowing particle exchange with fresh sample on a continuous basis. These attributes allow characterization of particle charge in a variety of industrial processes (9). In the production of potable water, the SCD has demonstrated a number of benefits, including reduced coagulant expenses and more consistent water quality. Its feasibility has recently been demonstrated in the automatic control of organic polyelectrolyte dosing prior to the full-scale dewatering of municipal sludges (7). In practice, process response to SCD control requires several minutes since the SCD does not reequilibrate instantaneously after a change in influent colloidal characteristics (4, 5).

It has been experimentally evident that a correlation exists between SCD output and measured zeta potentials (e.g., 3). Although quantified explanations of the SCD developed to date have predicted such a correlation, they have relied on simplifications due to the complexity of the involved phenomena. The original solution developed by Gerdes (10, 3) assumed a triangular fluid velocity profile within the annulus and a capacitor model of the electrical double layer. A later derivation (9) incorporated a more appropriate velocity profile and utilized the Debye-Hückel diffuse layer model but neglected inertial effects on annular flow. Both models provided analytical solutions that predicted linear relationships between particle zeta potential and measured streaming current. Experimental results confirmed the latter model to within 4% under controlled experimental conditions (9). Barron *et al.* (1) have recently published an equation that also predicts a linear relationship between zeta potential and

<sup>1</sup> To whom correspondence should be addressed.

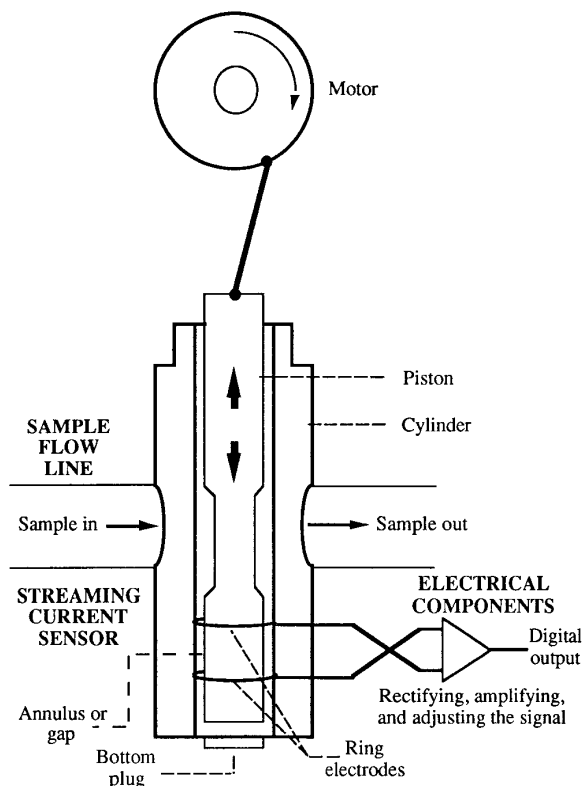


FIG. 1. Components of sensor used in streaming current detector.

streaming current under some conditions, but no details or experimental confirmation have been provided.

Nonideal phenomena within the sensor have also been identified that limit the adherence of SCD measurements to theoretical predictions. The following three idealizations are assumed in all models discussed in this paper.

(1) *Representative attachment*: The materials attaching to sensor surfaces within the annulus are assumed to be representative of the overall dispersed phase that would be subjected to other electrokinetic analyses for the determination of zeta potential.

(2) *Absence of electrical artifacts*: The electrical current measured from the electrodes in the SCD sensor is assumed to be free of electrical influences other than the alternating current generated by counterion migration.

(3) *Complete surface coverage*: Coverage of the sensor surfaces by colloidal material is assumed to be essentially complete; i.e., there are no bare surfaces. Consistent with the first assumption, if a coagulant or other adsorptive substance is used to modify colloidal properties, these colloids and/or the adsorbate must cover the sensor surfaces in a representative manner.

Generally, the most problematic assumption appears to be the third one listed above (e.g., 1, 3–5). Circumstances in which effects of nonideal behavior may arise under each of

the above categories are discussed in more detail elsewhere (6). Results have also been presented indicating apparent adherence to the above assumptions (9, 6).

## MATHEMATICAL DESCRIPTION OF THE STREAMING CURRENT DEVICE

The desired relationship is between the current generated in the SCD ( $i$ ) and the zeta potential ( $\zeta$ ). The geometry of a cross section normal to the axis of the piston and cylinder is defined in Fig. 2. The velocity of fluid flow in the axial direction ( $v$ ) must first be determined as a function of radial location. The product of this velocity and the space charge density ( $\rho$ ) provides the local flux of ionic charge, with an integration over the cross-sectional area between the cylinder and the piston then providing the overall streaming current that results:

$$i = \int_0^{2\pi} \int_{\lambda R}^R \rho(r)v(r)r dr d\phi. \quad [1]$$

Equations for the flow field  $v(r)$  and space charge density  $\rho(r)$  are developed in the following sections. In this derivation we assume an incompressible Newtonian fluid in the annulus and neglect end effects.

### Flow Field for Newtonian Fluid

*Exact solution with inertia in polar coordinates ( $v1$ )*. We consider flow in the gap between two concentric cylin-

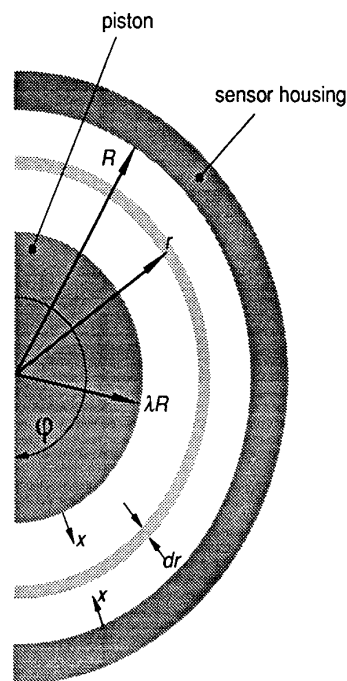


FIG. 2. Halved cross section of sensor with notation used in equations. Some SCD sensors include ridges or guide surfaces on the piston, which are not considered in this analysis.

ders, with the inner cylinder oscillating in the axial direction in a closed end cylinder. The axial velocity  $V(t)$  of the inner cylinder (piston) is prescribed. The outer cylinder is denoted  $R$  and the inner cylinder is  $\lambda R$ . In our previously reported results (9),  $\lambda$  takes on values between 0.9079 and 0.9831. Beginning with the Navier–Stokes equation in cylindrical components for the  $r$  component,

$$\begin{aligned} & \rho \left[ \frac{\partial v_r}{\partial t} + v_r \frac{\partial v_r}{\partial r} + v_\theta \frac{\partial v_r}{\partial \theta} + v_x \frac{\partial v_r}{\partial x} - \frac{v_\theta^2}{r} \right] \\ &= -\frac{\partial p}{\partial r} + \rho g_r + \mu \left[ \frac{\partial^2 v_r}{\partial r^2} + \frac{1}{r} \frac{\partial v_r}{\partial r} + \frac{1}{r^2} \frac{\partial^2 v_r}{\partial \theta^2} \right. \\ & \quad \left. + \frac{\partial^2 v_r}{\partial x^2} - \frac{v_r}{r^2} - \frac{2}{r^2} \frac{\partial v_\theta}{\partial \theta} \right]. \quad [2] \end{aligned}$$

Assuming viscous, parallel, time periodic flow with no swirl in the annulus, we may write the boundary value problem governing  $v(r, t)$ , the velocity in the annulus, as

$$\begin{aligned} \frac{\partial v}{\partial t} &= -\frac{1}{\rho} \frac{\partial p}{\partial x} + \frac{\nu}{r} \frac{\partial}{\partial r} \left( r \frac{\partial v}{\partial r} \right); \quad \lambda R \leq r \leq R \\ v(R, t) &= 0 \\ v(\lambda R, t) &= V(t), \quad [3] \end{aligned}$$

where the subscripts have been dropped and  $\nu$  is the kinematic viscosity. For simplicity denote  $F(t) = -(1/\rho)(\partial p/\partial x)$ , which is unknown at this point. We find  $F(t)$  by imposing large-scale mass conservation:

$$\pi(\lambda R)^2 V(t) = -2\pi \int_{\lambda R}^R v(r, t) r dr. \quad [4]$$

Assuming the motion to be purely harmonic, we take

$$\begin{pmatrix} v(r, t) \\ V(t) \\ F(t) \end{pmatrix} = \begin{pmatrix} \tilde{v}(r) \\ \tilde{V} \\ \tilde{F} \end{pmatrix} e^{i\omega t}, \quad [5]$$

which reduces the boundary value problem to

$$\begin{aligned} i\omega \tilde{v} &= \tilde{F} + \frac{\nu}{r} \frac{\partial}{\partial r} \left( r \frac{\partial \tilde{v}}{\partial r} \right); \quad \lambda R \leq r \leq R \\ \tilde{v}(R) &= 0 \\ \tilde{v}(\lambda R) &= \tilde{V} \\ \int_{\lambda R}^R \tilde{v}(r) r dr &= -\frac{(\lambda R)^2}{2} \tilde{V}. \quad [6] \end{aligned}$$

We nondimensionalize  $r$  by  $R$  and the velocity in the gap by  $\tilde{V}$ ;

$$r' = \frac{r}{R}; \quad v' = \frac{\tilde{v}}{\tilde{V}}. \quad [7]$$

Substituting these into the boundary value problem equations and dropping the primes gives

$$\begin{aligned} r \frac{\partial^2 v}{\partial r^2} + \frac{\partial v}{\partial r} - \left( \frac{R}{\delta} \right)^2 r v &= -K \left( \frac{R}{\delta} \right)^2 r; \quad \lambda \leq r \leq 1 \\ v(1) &= 0 \\ v(\lambda) &= 1 \quad [8] \end{aligned}$$

$$\int_{\lambda}^1 v(r) r dr = -\frac{\lambda^2}{2}, \quad [9]$$

where  $\delta = (\nu/\omega)^{1/2}$  is a boundary layer thickness and

$$K = \frac{\tilde{F}}{\omega \tilde{V}}. \quad [10]$$

This equation may be put in standard form by the transformation

$$z = \frac{R}{\delta} r, \quad [11]$$

which gives

$$z \frac{\partial^2 v}{\partial z^2} + \frac{\partial v}{\partial z} - izv = -Kz. \quad [12]$$

The homogeneous solution of Eq. [12] is written as

$$v_H(z) = c_1(\text{ber}(z) + i \text{bei}(z)) + c_2(\text{ker}(z) + i \text{kei}(z)), \quad [13]$$

where

$$\begin{aligned} \text{ber}(z) + i \text{bei}(z) &= J_0(i^{3/2}z) \\ \text{ker}(z) + i \text{kei}(z) &= K_0(i^{1/2}z). \quad [14] \end{aligned}$$

We use the Bessel function with complex arguments from here on. This form is handled properly by *Mathematica*, which was used to do all the calculations presented here. The solution is given by

$$v(r) = c_1 \left( \frac{R}{\delta}, \lambda, K \right) J_0 \left( i^{3/2} \left( \frac{R}{\delta} \right) r \right) + c_2 \left( \frac{R}{\delta}, \lambda, K \right) K_0 \left( i^{1/2} \left( \frac{R}{\delta} \right) r \right) - iK, \quad [15]$$

where

$$\begin{aligned} c_1 &= D^{-1} \left[ iKK_0 \left( i^{1/2} \lambda \frac{R}{\delta} \right) - (1 + iK)K_0 \left( i^{1/2} \frac{R}{\delta} \right) \right] \\ c_2 &= D^{-1} \left[ (1 + iK)J_0 \left( i^{3/2} \frac{R}{\delta} \right) - iKJ_0 \left( i^{3/2} \lambda \frac{R}{\delta} \right) \right] \\ D &= J_0 \left( i^{3/2} \frac{R}{\delta} \right) K_0 \left( i^{1/2} \lambda \frac{R}{\delta} \right) - J_0 \left( i^{3/2} \lambda \frac{R}{\delta} \right). \quad [16] \end{aligned}$$

We now apply the condition [9] to eliminate  $K$ . This gives

$$c_1(K)I_1 + c_2(K)I_2 - iK \frac{(1 - \lambda^2)}{2} = -\frac{\lambda^2}{2}, \quad [17]$$

where

$$\begin{aligned} I_1 &= \int_{\lambda}^1 J_0 \left( i^{3/2} \frac{R}{\delta} r \right) r dr \\ &= i^{5/2} \left( \frac{R}{\delta} \right)^{-1} \left[ J_1 \left( i^{3/2} \frac{R}{\delta} \right) - \lambda J_1 \left( i^{3/2} \frac{R}{\delta} \lambda \right) \right] \\ I_2 &= \int_{\lambda}^1 K_0 \left( i^{1/2} \frac{R}{\delta} r \right) r dr \\ &= i^{3/2} \left( \frac{R}{\delta} \right)^{-1} \left[ K_1 \left( i^{1/2} \frac{R}{\delta} \right) - \lambda K_1 \left( i^{1/2} \frac{R}{\delta} \lambda \right) \right]. \quad [18] \end{aligned}$$

Noting that  $c_1$  and  $c_2$  are linear functions of  $K$ , and by rearranging Eq. [17] and solving for  $K$ ,

$$K = \frac{(\lambda^2/2) + c_{10}I_1 + c_{20}I_2}{(i/2)(1 - \lambda^2) - c_{11}I_1 - c_{21}I_2}, \quad [19]$$

where

$$\begin{aligned} c_{10} &= -D^{-1}K_0 \left( i^{1/2} \frac{R}{\delta} \right) \\ c_{20} &= -D^{-1}J_0 \left( i^{3/2} \frac{R}{\delta} \right) \\ c_{11} &= iD^{-1} \left[ K_0 \left( i^{1/2} \lambda \frac{R}{\delta} \right) - K_0 \left( i^{1/2} \frac{R}{\delta} \right) \right] \\ c_{21} &= iD^{-1} \left[ J_0 \left( i^{3/2} \frac{R}{\delta} \right) - J_0 \left( i^{3/2} \lambda \frac{R}{\delta} \right) \right]. \quad [20] \end{aligned}$$

This solution is compared to several approximations below.

*Approximate solution: no inertia, with polar coordinates (v2).* A previous solution of the flow field in the no-inertia limit has been described by Elicker *et al.* (9). The solution may be written as

$$v(r) = A(1 - \lambda^2) - [A(1 - \lambda^2) - 1] \frac{\ln(r)}{\ln(\lambda)}, \quad [21]$$

where

$$A = \frac{K}{4} \left( \frac{R}{\delta} \right)^2. \quad [22]$$

Solving for  $K$  by the criteria above gives

$$K = \frac{4(\delta/R)^2}{(1 - \lambda^2) + \ln \lambda(1 + \lambda^2)}. \quad [23]$$

*Approximate solution: inertia with Cartesian coordinates (narrow gap approximation, (v3)).* Another approximation to the full solution is given by a small-gap ( $\lambda$  close to 1) approximation. For the narrow limit, we take  $y$  to denote distance away from the cylinder and assume that the annular region may be approximated by a region between two flat plates. The resulting boundary value problem is given by

$$\begin{aligned} iv(y) - \left( \frac{\delta}{R} \right)^2 \frac{d^2v}{dy^2} &= -K \\ v(0) &= 1 \\ v(1 - \lambda) &= 0. \quad [24] \end{aligned}$$

The solution is given by

$$v(y) = d_1 \cosh[\sqrt{a} y] + d_2 \sinh[\sqrt{a} y] - iK, \quad [25]$$

where

$$\begin{aligned} a &= i \left( \frac{R}{\delta} \right)^2 \\ d_1 &= 1 + iK \\ d_2 &= -\frac{\cosh[\sqrt{a}(1 - \lambda)]}{\sinh[\sqrt{a}(1 - \lambda)]} + iK \frac{(1 - \cosh[\sqrt{a}(1 - \lambda)])}{\sinh[\sqrt{a}(1 - \lambda)]}. \quad [26] \end{aligned}$$

The large-scale mass conservation requirement is approximated as

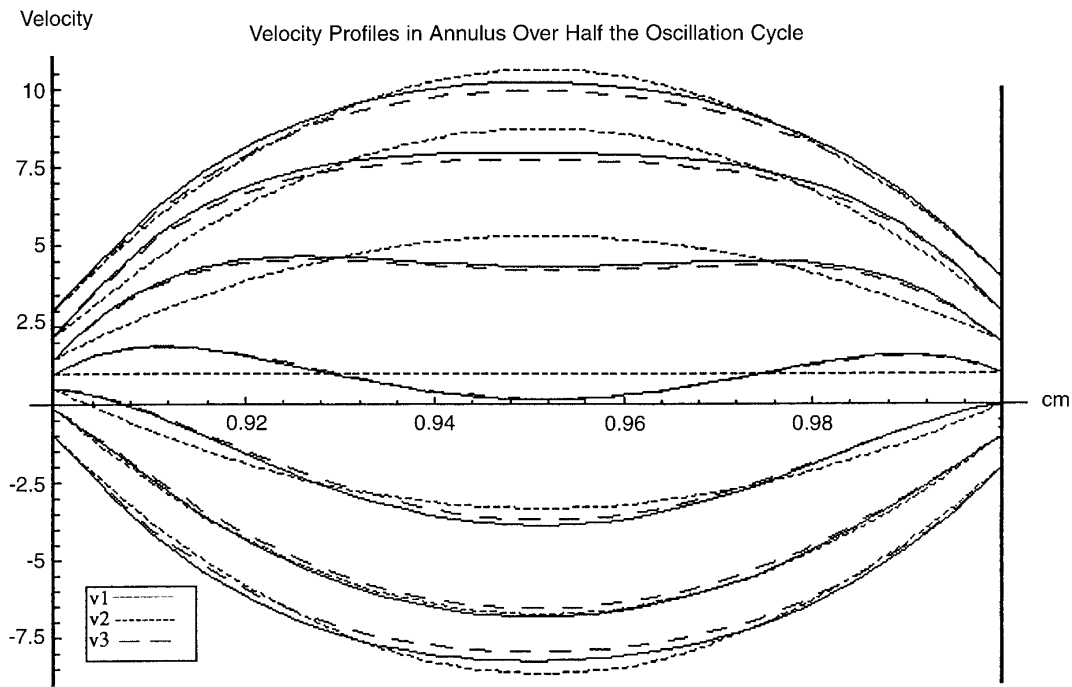


**FIG. 3.** Flow profiles in the annulus of the SCD as predicted by the full solution ( $v_1$ ), the no inertia solution ( $v_2$ ), and the inertial narrow gap solution ( $v_3$ ) at phases differing by  $\pi/6$  for one-half the oscillation cycle. Abscissa indicates distance  $r$  from the center of the piston, with an outer radius of 1 cm.

$$\int_0^{1-\lambda} v(y) dy = -\frac{\lambda^2}{2}, \quad [27]$$

which gives, finally,

$$K = -\frac{(\lambda^2/2) \sqrt{a} + d_{11} \sinh[\sqrt{a}(1-\lambda)] + d_{21} (\cosh[\sqrt{a}(1-\lambda)] - 1)}{d_{12} \sinh[\sqrt{a}(1-\lambda)] + d_{22} (\cosh[\sqrt{a}(1-\lambda)] - 1) - i\sqrt{a}(1-\lambda)}$$

$$d_{11} = 1$$

$$d_{12} = i$$

$$d_{21} = -\frac{\cosh[\sqrt{a}(1-\lambda)]}{\sinh[\sqrt{a}(1-\lambda)]}$$

$$d_{22} = i \frac{(1 - \cosh[\sqrt{a}(1-\lambda)])}{\sinh[\sqrt{a}(1-\lambda)]}. \quad [28]$$

#### Comparisons of Flow Fields for the Three Solutions

A comparison of the full solution ( $v_1$ ) to the no inertia solution ( $v_2$ ) and to the inertial solution in Cartesian coordinates ( $v_3$ ) is given in Fig. 3. The set of curves representing the most negative velocities are the instantaneous velocity profiles for the  $v_1$ ,  $v_2$ , and  $v_3$  solutions at  $t = 0$ , with the piston accordingly moving upward at midstroke. The six

subsequent set of curves represent the instantaneous velocity profiles for the  $v_1$ ,  $v_2$ , and  $v_3$  solutions at  $\pi/6$  intervals, totaling one-half an oscillation cycle. The leftmost boundary represents the moving piston, while the rightmost boundary represents the stationary cylinder with the gap width corresponding to the horizontal axis. The vertical axes of the  $t = 0, \pi/6, \pi/3, \pi/2, 2\pi/3, 5\pi/6,$  and  $\pi$  sets of curves have been displaced  $-2, -1, 0, 1, 2, 3,$  and  $4$  units, respectively, to facilitate comparisons, through an offset superimposition of the three velocity profiles during the oscillation cycle. Thus only the  $\pi/3$  phase has its true vertical axis.

The figure shows that the no-inertial solution provides a poor representation of the flow field for the parameters presented here ( $\omega = 2\pi 5$  rad/s,  $\lambda = 0.9$ ,  $R = 1$  cm,  $T = 20^\circ\text{C}$ , with the velocity represented nondimensionally on the  $y$ -axis). Of particular note is the region close to the bounding walls. This region will ultimately determine the current generated because this is where the charge distribution is concentrated. For the middle third of the piston's upward or downward excursions, the two inertial solutions ( $v_1$  and  $v_3$ ) are significantly advanced with respect to the no-inertia solution ( $v_2$ ). This discrepancy will cause erroneous predictions of instantaneous streaming current using  $v_2$ , although the effect of time-averaging over the complete piston cycle will be shown to mitigate this error. This occurs because, in the time-averaging or rectification process accomplished by the SCD circuitry, it is the absolute magnitude of the velocity

near the charged surface that ultimately influences the current produced. Figure 3 shows that the absolute velocity for  $v_2$  is too high for the first three phases pictured but too low for the last four phases compared to  $v_1$  and  $v_3$ , leading to a smaller net error.

The differences between the two inertial solutions,  $v_1$  and  $v_3$ , are negligible near the bounding walls. It is also seen that the narrow gap approximation,  $v_3$ , provides a reasonably accurate description of the full solution,  $v_1$ , throughout the piston cycle. Nevertheless, the difference between the inertial solutions increases as the amplitude of the velocity profile increases, with the greatest difference occurring at mid-gap width for every phase. The particular phases of greatest difference between the inertial solutions are the  $t = 0$  and  $\pi$  phases, or midstroke of the piston's upward and downward movement. Figure 3 shows that the narrow gap solution always gives the absolute magnitude of the flow velocity to be somewhat less than does the full solution.

Temperature greatly influences differences between the no-inertia and the inertia solutions. As temperature decreases, the viscosity of the water increases, thus increasing the viscous forces at the expense of the acceleration or inertial forces. The Reynolds number estimates the ratio of the inertial forces to the viscous forces and may be defined here as

$$\text{Re} = \frac{R(1 - \lambda) \left[ \frac{s\omega}{2} v(r) \right]}{\nu}, \quad [29]$$

where

- $s$  = the piston stroke length,
- $\omega$  = the piston frequency in rad/s, and
- $v(r)$  = the exact solution as previously defined in [15].

This is a local Reynolds number and is determined at the time and location of greatest fluid velocity. *Mathematica* computes the bracketed term to facilitate determination of the local Reynolds number. Using this definition and standard streaming current detector parameters ( $\omega = 2\pi(4.83)$  rad/s,  $\lambda = 0.9831$ ,  $R = 0.9376$  cm), a temperature decrease from 25 to 5°C was found to decrease the Reynolds number 41%, demonstrating the increased importance of the viscous forces and the decreased importance of the inertial forces. The consequence of the temperature decrease is to bring the no-inertia solution ( $v_2$ ) into closer similitude with the inertial solutions  $v_1$  and  $v_3$ . Of final note, the Reynolds number calculations showed that flow in the annulus is always in the laminar range. The highest predicted local Reynolds number was determined to be 748, for standard streaming current parameters at a water temperature of 25°C.

### Charge Density Distribution

In order to obtain  $\rho(r)$ , the one-dimensional Poisson–Boltzmann equation for symmetrical electrolytes is specified

$$\nabla^2 \psi = \frac{d^2 \psi}{dr^2} = -\frac{\rho(r)}{\epsilon} = \frac{2ze_0 n_0}{\epsilon} \sinh\left(\frac{ze\psi}{kT}\right), \quad [30]$$

with

- $\psi$  = electrical potential,
- $r$  = distance from surface,
- $\epsilon$  = dielectric constant,
- $z$  = magnitude of electrolyte charge,
- $e_0$  = fundamental electric charge,
- $n_0$  = bulk solution electrolyte concentration,
- $k$  = Boltzmann constant, and
- $T$  = absolute temperature.

The derivation is limited to a symmetrical electrolyte by the above equation. The assumptions of one dimensionality and use of the radial coordinate ( $r$ ) are reasonable for the systems characterized here given that the product  $\kappa\lambda R > 10^7$ , where  $\kappa$  is the inverse double-layer dimension (11). The equation can be integrated to give

$$\tanh\left(\frac{ze_0\psi(r)}{4kT}\right) = \tanh\left(\frac{ze_0\zeta}{4kT}\right) \exp(-\kappa r). \quad [31]$$

The usual boundary condition used to arrive at Eq. [31] was slightly modified for the present purposes, with the boundary electrical potential specified by the zeta or shear plane potential ( $\zeta$ ) instead of the surface potential  $\psi_0$ . This provides the same boundary location used for the flow field description.

Solving for  $\psi(r)$  and substituting into Eq. [30] returns the space charge density as a function of distance from the shear plane:

$$\rho(r) = -2ze_0 n_0 \sinh\{4 \tanh^{-1} [\tanh(ze_0\zeta/4kT) \exp(-\kappa r)]\}. \quad [32]$$

### Combined Model to Solve for Streaming Current

The appropriate equations for fluid velocity and charge density from the preceding sections are then combined and integrated in Eq. [1] to solve for the streaming current. A program was created using *Mathematica* for this purpose. The program requires parameters describing the streaming current device ( $\omega$ ,  $\lambda$ , and  $R$ ) and characteristics of the solution (ionic strength and temperature, which determine both the viscosity and dielectric constant). For an assumed zeta potential the equations are numerically integrated over the annular cross section to provide current as a function of time. The current is then rectified and time averaged.

In order to increase the program's computational speed, the flow velocity equation was simplified by power series expansion and use of leading terms only. This is possible because the charge density of counterions is only significant relatively close to the shear plane. Thus the distances of importance for the generation of the streaming current are in the nanometer range, and details of the velocity profile further into the gap width, which is in the millimeter range, are unimportant.

The number of expansion terms used in the computation was first varied in order to determine any loss of accuracy resulting from the use of fewer terms. However, reductions in the number of terms were seen to produce insignificant differences in the current generated. A series of order one agreed with a series of order four to more than six significant digits. Thus only one term was used in the series expansion to facilitate program execution.

In the SCD, the oscillating current is either sampled periodically (e.g., at each  $\pi/2$  phase) or rectified continuously, depending on the circuitry employed. A time-smoothed value is provided as output which is indicative of the sign and amplitude of the characterized current, and therefore of the zeta potential. The program simulates the continuous rectification method of determining current magnitude, which is used by many SCDs to avoid false readings due to phase shift. Interestingly, a false reading due to periodic sampling is predicted by the program because the inertial forces create a phase lag between the piston motion and current signal. The degree of phase lag varies with both streaming current detector parameters and solution characteristics.

The program was used to create graphs of flow velocity, charge density, and charge flux with distance from the bounding surfaces at various phases of the oscillation cycle, and current or time-rectified current over the oscillation cycle. Finally, the program determined time-averaged current magnitude for the complete solutions of the inertial or no inertial flows with the charge density distribution Eq. [32], and also for appropriate approximations of both the flow and the charge density distribution.

## STREAMING CURRENT RESULTS

### *Current vs Zeta Potential: Comparison of Solutions*

The following results show predicted streaming current as a function of zeta potential utilizing four different mathematical descriptions. The first is the full solution of the flow field (*i1*), the second is the no-inertia flow field (*i2*), and the third is the narrow gap approximation (*i3*). Equation [31] has been utilized for the space charge density for these three descriptions. The fourth solution (*i4*) is the original solution that relies on somewhat simplistic assumptions, such as a triangular fluid velocity profile and a capacitor

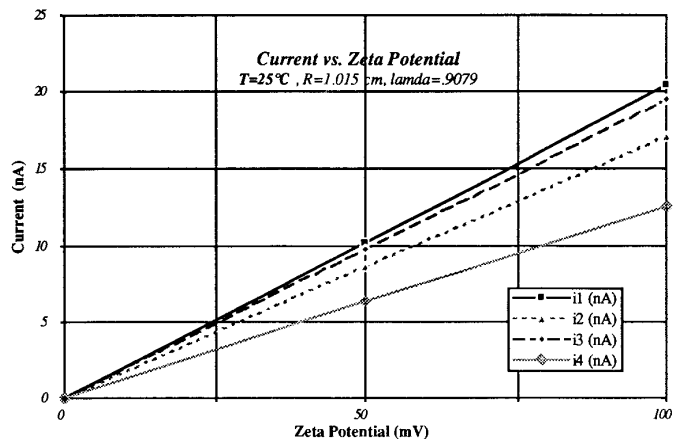


**FIG. 4.** Current vs zeta potential for large gap sensor at 25°C. Assumed values were: cylinder radius, 1.015 cm; gap ratio, 0.9079; piston frequency,  $2\pi$  (4.83) rad sec<sup>-1</sup>; fluid viscosity, 0.0089 g cm<sup>-1</sup> s<sup>-1</sup>; fluid density, 0.997 g cm<sup>-3</sup>; dielectric constant, 78.25; ionic strength, 0.01.

model of the electrical double layer (10, 3). The fourth solution can be represented as follows:

$$\bar{i} = \frac{8s\omega\epsilon}{(1-\lambda)^2} \zeta = \frac{4\tilde{V}\epsilon}{(1-\lambda)^2} \zeta, \quad [33]$$

where

$$\tilde{V} = \text{as defined in Eq. [5].}$$

Results using these four solutions can now be compared. The accuracy of approximations *i2*, *i3*, and *i4* may vary with sensor gap dimensions and temperature (with the latter due to viscosity differences). Thus, comparisons are presented for cases of both large and small gaps, and for temperatures of 25 and 5°C. Properties of dilute aqueous suspensions are assumed for these computations.

*Large gap, 25°C.* Solution (*i4*) explicitly predicts a linear relationship between the zeta potential and the generated current. As shown in Fig. 4, our computer-generated solutions for *i1*, *i2*, and *i3* essentially yield the same type of linear relationship, although the proportionality between the two quantities differs. The new solutions *i1* and *i3*, which account for inertial effects in the flow field, predict the greatest current for a given zeta potential. In particular the *i1* full solution predicts a current 18.8% higher than the no inertia *i2* solution.

This result stems from the particular conditions chosen for this comparison. Both the relatively large gap dimension,  $\lambda = 0.9079$ , and the relatively high water temperature, 25°C, allow the inertial forces to have a pronounced effect. The effect manifests itself by producing increased time-averaged flow field velocities when compared with the no-inertia time-averaged flow field velocities. An increased flow field velocity generates a higher current as the graph depicts.

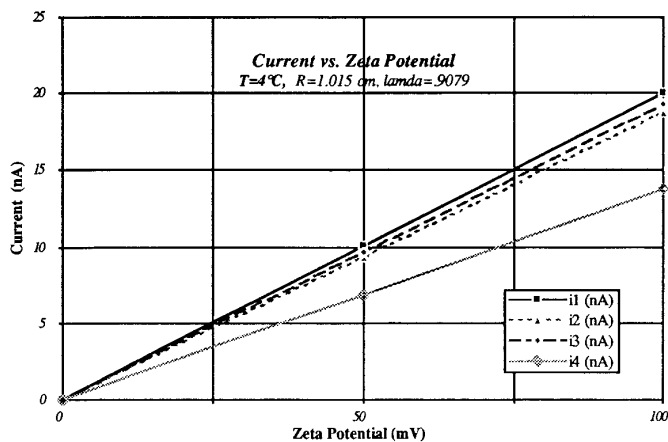


FIG. 5. Current vs zeta potential for large gap sensor at 4°C. Assumed values were as in Fig. 4 but using aqueous properties at 4°C: viscosity,  $0.0156 \text{ g cm}^{-1} \text{ s}^{-1}$ ; density,  $1.00 \text{ g cm}^{-3}$ ; and dielectric constant, 85.54.

*Large gap, 4°C.* The effect of a temperature decrease to 4°C can be seen in Fig. 5. The lower temperature, which might be encountered in water treatment applications, brings the inertia and no-inertia solutions into closer agreement. The temperature drop causes the fluid viscosity to increase, increasing the importance of viscous forces with respect to inertial forces. Nevertheless, the incorporation of inertial effects in the solution still increases the predicted current by 6.9%.

Although the full solution shows a current decrease of less than 1.6% due to the temperature decrease, the net effect on the time-averaged current actually results from an increase in the charge density, counteracted in Eq. [1] by a more significant increase in fluid velocity. A temperature decrease increases the charge density,  $\rho(r)$ , through both the effect of an increased  $\epsilon_{\text{rel}}$  on the inverse double-layer thickness and a decreased  $T$  on the argument of the hyperbolic terms in Eq. [32]. Conversely, the temperature drop decreases the absolute magnitude of the flow field velocity as seen graphically in the *Mathematica* program. Because the  $v_1$  and  $v_3$  inertial flow field velocities are noticeably greater than the  $v_2$  no-inertia flow field velocity at the higher temperature, the temperature-driven decrease in flow field velocity is significantly less for the no-inertia solution. This explains the decreased current of the  $i_1$  and  $i_3$  solutions and the increased current of the  $i_2$  and  $i_4$  solutions from Fig. 4 to Fig. 5. The decrease in the inertial flow field velocity for the  $i_1$  and  $i_3$  solutions more than offsets the increase in charge density, acting to reduce the time-averaged current. The  $i_2$  and  $i_4$  solutions, however, predict the flow velocity decrease to be less consequential than the charge density increase.

*Small gap, 25°C.* The effect of a decrease in the gap dimension of the SCD's sensor can be seen in Fig. 6. This figure interestingly uses standard SCD gap dimensions ( $R$

= 0.9376 cm,  $\lambda = 0.9831$ ). The advantage of the smaller gap is seen to be a significant increase in the current generated, which stems from the higher fluid velocities in the smaller cross-section. These results were computed for conditions at 25°C, so no temperature effects are included relative to Fig. 4. Comparison with Fig. 5 shows that the decreased gap width leads to a convergence of the inertia and no-inertia solutions to a more dramatic extent than from the temperature decrease. The gap is so small that the inertial forces are severely restrained by the viscous forces and, as a consequence, the inertia and no-inertia solutions are essentially the same, with  $i_1$  and  $i_2$  corresponding to within 2/100 of 1%. Thus, for the standard SCD, these results support the accuracy of the no-inertia approximation reported by Elicker *et al.* (9).

The smaller cylinder radius and gap width also increases the relative curvature of the gap, worsening the validity of the Cartesian approximation. In other words, it becomes less satisfactory to approximate the annular region as a region between two flat plates. Consequently, the  $i_3$  solution in Fig. 6 deviates from the  $i_1$  full solution even more than does the  $i_2$  no-inertia solution. In all cases the simplistic model developed by Gerdes ( $i_4$ ) gives an approximation predicting the current to be considerably less than shown by the more exact solutions.

*Small gap, 4°C.* These results, not presented in a figure, give even closer agreement between solutions  $i_1$ ,  $i_2$ , and  $i_3$  than in Fig. 6. Thus, for applications at temperatures less than 25°C, as common in potable water treatment, the three solutions are quite equivalent. The program also predicts increasing current with decreasing temperature for standard SCD parameters, as has been experimentally observed (8). The theoretical reasoning for this was explained previously.

#### Evaluation of Analytical Solution for $i_2$

The equations used for the no-inertia case can be simplified further to provide an analytical solution for the current.

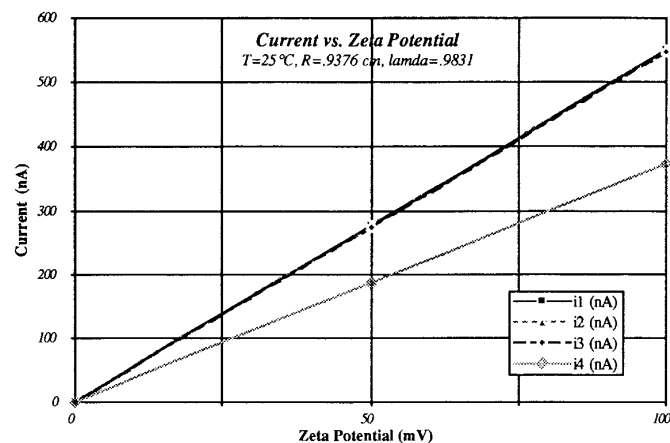
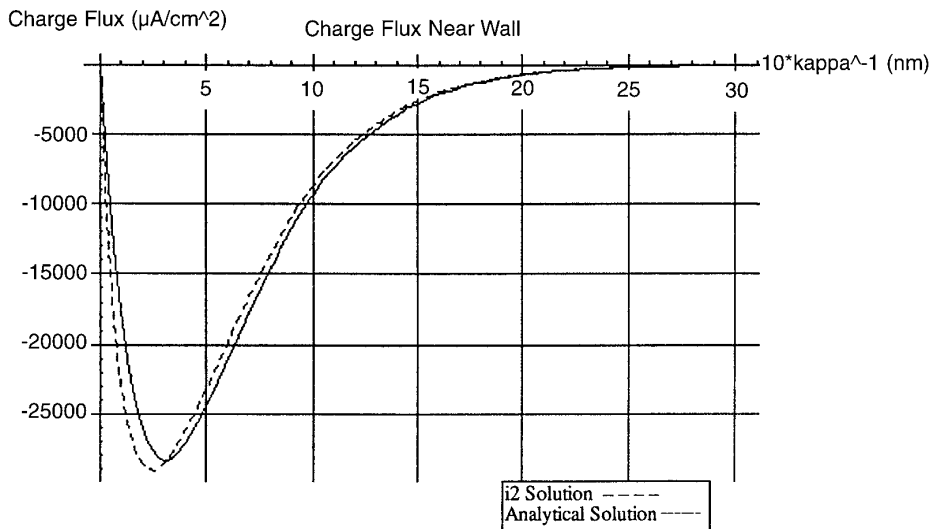


FIG. 6. Current vs zeta potential for small gap sensor at 25°C. Assumed values as in Fig. 4 but for an SCD with a cylinder radius of 0.9376 cm and gap ratio of 0.9831.



**FIG. 7.** Comparison of charge fluxes as predicted by the  $i_2$  solution and the analytical solution over ten times the electrical double layer dimension  $1/\kappa$ , for conditions as in Fig. 6.

A first-order approximation for the velocity profile is employed, as justified in our numerical comparisons varying the number of expansion terms utilized. The Debye–Hückel approximation for the charge density is also used, which is a simplification of Eq. [32], valid for low potentials:

$$\rho(r) = -\kappa^2 \epsilon \zeta \exp(-\kappa r). \quad [34]$$

Using these simplifications, we have previously shown (9) the analytical solution to be

$$\begin{aligned} \bar{i} &= 4s\omega\epsilon\zeta / \left(1 + \frac{1 + \lambda^2}{1 - \lambda^2} \ln \lambda\right) \\ &= 2\tilde{V}\epsilon\zeta / \left(1 + \frac{1 + \lambda^2}{1 - \lambda^2} \ln \lambda\right). \quad [35] \end{aligned}$$

This  $i_2$  approximation was compared to the *Mathematica* program's numerical solutions for  $i_1$  and  $i_2$  and was found to agree with both to four significant digits for the narrow gap, 25°C case. This equation is therefore reasonably accurate for common conditions and is maintained at decreasing temperatures. Nevertheless, the *Mathematica* program also shows that some of this solution's accuracy is fortuitous. Though the velocity profile approximation is valid, the charge density approximation (Eq. [34]) leads to some error in the charge flux, as quantified in Fig. 7. Using the conditions of Fig. 6 and a  $\zeta$  of 50 mV, this figure compares the time-averaged charge flux over 10 times the EDL dimension (i.e.,  $10/\kappa$ ) for the  $i_2$  solution and the analytical solution. The Debye–Hückel charge density approximation undercompensates the charge flux near the charged coated wall and overcompensates the charge flux further from the wall.

The overall outcome, however, masks the local differences and gives a result that is essentially the same as the more elaborate solutions  $i_1$ ,  $i_2$ , and  $i_3$ .

In our previous work, comparisons of zeta potentials measured by SCD and by electrophoretic mobility showed agreement of Eq. [35] with experimental results to within 4% (9). This degree of accuracy has been confirmed in more recent experimental comparisons, to be reported elsewhere. For standard SCD configurations, the differences between  $i_1$ ,  $i_2$ ,  $i_3$ , and the analytical solution were less than inherent experimental error, but with increasing  $R$  or  $\lambda$ , the superior accuracy of the  $i_1$  solution became obvious. Thus the analytical expression is only valid for selected conditions, although these include conventional sensor dimensions and application temperatures. Analogous restrictions will apply to the  $i_2$  solution.

#### Evaluation of Phase Shift Prediction

Previous experimental observations by oscilloscope showed that, under some conditions, the alternating current obtained from the SCD sensor was out of phase with the sinusoidal motion of the piston itself. This variable phase lag in the SCD detector is quantified by the program. Previous literature hypothesized that high concentrations of electrolytes in solution may cause capacitive effects of oriented ions near the electrode surfaces or other rate limitations in the half reactions occurring at the electrodes (6). However, this model gives an alternative physical explanation for the observed phase shifts.

Figure 8 illustrates the phase lag observed in the SCD for a  $\zeta$  potential of  $-50$  mV, with other conditions as previously used in Fig. 4 (large gap, 25°C). The piston frequency of 4.83 cycles per second gives the indicated oscillation period

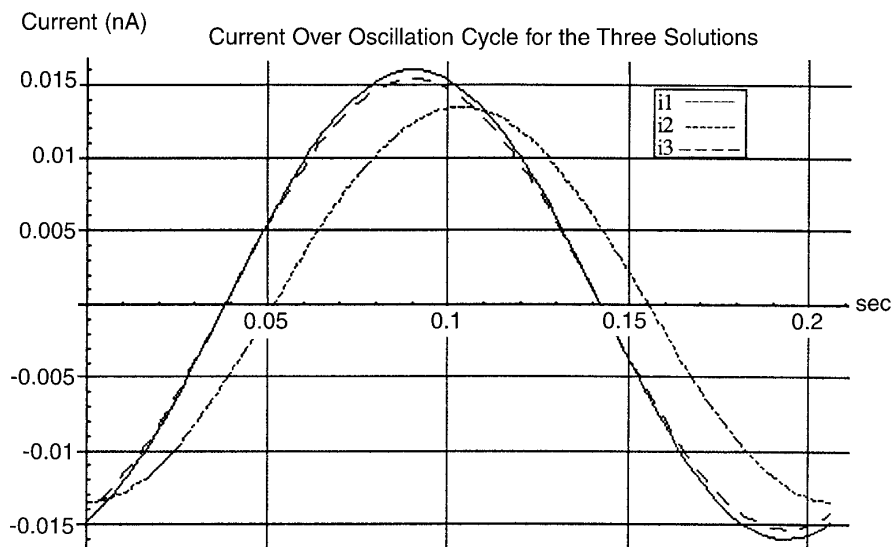


FIG. 8. Current over oscillation time for the  $i_1$ ,  $i_2$ , and  $i_3$  solutions with same parameter values given for Fig. 4 and  $\zeta = -50$  mV.

of 0.0207 s. A  $25.2^\circ$  phase lag for  $i_1$  and  $i_3$  occurs because of the role of inertial (acceleration) forces in this system, as described previously. Since the  $i_2$  solution assumes no inertial effects, no phase lag is predicted.

As discussed previously, different methods are available by which the signal processing component of the SCD may convert the time-variant streaming current into a continuous readout that is only a function of the signal amplitude. Under conditions where phase lag may be encountered (e.g., with higher viscosity suspensions or sludges), Fig. 8 shows that continuous, polarity-sensitive rectification of the signal will provide much less error than periodic sampling of the amplitude, as practiced in older SCD models. A constant delay time in sampling will not correct the error properly, since the phase shift is a function of sample viscosity, which may vary.

The phase shift effect decreases with lower temperature or smaller gap size. Assuming the same SCD parameters used in Fig. 5 (large gap, but at  $4^\circ\text{C}$ ) decreased the phase lag to  $16.5^\circ$ , a result of the viscous forces harnessing the inertial terms. Using the conditions of Fig. 6 (small gap,  $25^\circ\text{C}$ ), the phase lag became negligible as the inertial terms have a greatly diminished role for this system. This will also be the case for a small gap at  $4^\circ\text{C}$ .

#### Use of SCD Measurements

The predicted output of the model, the time-averaged current generated in the annulus, is related to the actual reading of an SCD through an amplification factor

$$SC = K_{amp}i, \quad [36]$$

where  $K_{amp}$  is the product of gains through several stages of

electrical processes and must be determined through empirical testing or circuit analysis for the SCD device. This value would be useful in order to determine the actual current ( $i$ ) when the SCD reading (SC) is known, or to determine the zeta potential when the measured SC is known. Alternatively, the SCD reading may be calibrated to material with a predetermined zeta potential (8).

The mathematical derivations described here, and the essentially linear streaming current–zeta potential relationship that is arrived at, assume certain idealizations in the workings of the SCD. As previously described (6), these idealizations are representative attachment, absence of electrical artifacts, and complete surface coverage. Failing these assumptions, as documented in some cases, the instrument will provide only a qualitative indicator of zeta potential. Such a qualitative measure is sufficient for successful process control in practical applications (3, 2) but is unsatisfactory for analytical applications. On the other hand, successful experimental verification of the analytical solution (9) indicates that the required assumptions, such as that of complete surface coverage, are supportable under specific conditions.

## CONCLUSIONS

An improved theoretical model of the SCD, which includes inertial flow effects, the proper cylindrical sensor geometry, and a precise electrical double-layer description, allows rigorous calculation of the streaming current generated with specified sensor dimensions and solution conditions. A uniform zeta potential on inner sensor surfaces or adsorbed material is assumed.

With a relatively large annular gap, and at a temperature of  $25^\circ\text{C}$ , the fluid velocity profile between the cylinder and

piston includes a significant component attributable to inertial forces. Under such conditions, a solution that neglects these effects provides an inaccurate prediction of the flow field. A smaller gap size—as used in commercial SCDs—diminishes the inertial component and improves the accuracy of the noninertial solution. A decrease in temperature to 4°C has the same effect, due to the increase in fluid viscosity.

A Cartesian approximation for the SCD sensor's geometry, with inertial effects accounted for, gives a solution for annular velocity that is accurate for large gap dimensions relative to the radius of curvature. The solution becomes less accurate than the noninertial radial solution when the gap is decreased to the small width typical of standard SCD sensors.

The solutions that incorporate inertial effects show that this factor gives rise to a phase lag in current relative to piston motion. The effect is substantial with wide annular dimensions, still significant at decreasing temperatures, but negligible with the smaller gap width of commercial SCDs, provided that the sample viscosity is similar to that of water.

Decreasing the sensor's gap width causes a significant increase in the current generated by the SCD. A decrease in temperature causes little change in current with a wide gap, but a more significant increase with the smaller, conventional annular gap.

Only the fluid velocities relatively close to the annular boundaries play a role in determining the charge flux in the sensor. A linear approximation for the velocity profile near these boundaries can be used in determining the streaming current, with minimal loss of accuracy.

Use of the Debye–Hückel charge density approximation

leads to a slight error in the predicted spatial distribution of charge flux, but allows an analytical solution for sensor current that is accurate under conventional conditions for use of the SCD.

Time averaging of the streaming current's magnitude by polarity-sensitive rectification will decrease errors if a phase shift of the streaming current occurs. Such circuitry may be called for when characterizing high-viscosity samples.

## REFERENCES

1. Barron, W., Murray, B. S., Scales, P. J., Healy, T. W., Dixon, D. R., and Pascoe, M., *Colloids Surf. A* **88**, 129–139 (1994).
2. Dentel, S. K., and Abu-Orf, M. M., "Laboratory and Full-Scale Studies of Liquid Stream Viscosity and Streaming Current for Characterization and Monitoring of Dewaterability," *Water Res.* **29**, 2663–2672 (1995).
3. Dentel, S. K., and Kingery, K. M., "Using Streaming Current Detectors in Water Treatment," *J. Am. Water Works Assoc.* **81**, 443 (1989).
4. Dentel, S. K., Thomas, A. V., and Kingery, K. M., *Water Res.* **23**, 413–421 (1989).
5. Dentel, S. K., Thomas, A. V., and Kingery, K. M., *Water Res.* **23**, 423–430 (1989).
6. Dentel, S. K., *J. Water SRT-Aqua* **44**, 70–79 (1995).
7. Dentel, S. K., Abu-Orf, M. M., and Griskowitz, N. J., "Polymer Characterization and Control in Biosolids Management." Water Envt. Research Foundation, Alexandria, VA, 1995.
8. Elicker, M. L., "Fundamental Aspects of Streaming Current Detection," Master's thesis, University of Delaware, Newark, DE, 1990.
9. Elicker, M. L., Resta, J. J., Hunt, J. W., and Dentel, S. K., in "Chemical Water and Wastewater Treatment II" (R. Klute and H. Hahn, Eds.). Springer Verlag, Berlin, 1992.
10. Gerdes, W. F., "A New Instrument—The Streaming Current Detector. 12th National Analysis Instrument Symposium, Houston, TX, May, 1966."
11. Hunter, R. J., "Introduction to Modern Colloid Science." Oxford Univ. Press, Oxford, 1993.